MOLECULAR IMAGING AND BIOLOGY

Mol Imaging Biol (2019) 21:447–453
DOI: 10.1007/s11307-018-1250-7

Published Online: 9 August 2018

BRIEF ARTICLE

Sparse Detector Configuration in SiPM Digital Photon Counting PET: a Feasibility Study

Jun Zhang, Michelle I. Knopp, Michael V. Knopp

Wright Center of Innovation in Biomedical Imaging, Department of Radiology, The Ohio State University Wexner Medical Center, 395 W. 12th Avenue, Room 430, Columbus, OH, 43210, USA

Abstract

Purpose: To investigate the minimum number of SiPM detectors required for solid-state digital photon counting (DPC) oncologic whole-body 2-deoxy-2-[^{18}F]fluoro-D-glucose ([^{18}F]FDG) positron emission tomography (PET)/X-ray computed tomography (CT).

Procedures: A DPC PET/CT (Vereos, Philips) with 23,040 1-to-1 crystal-to-detector couplings was utilized. [^{18}F]FDG PET/CT of a uniformity phantom and 10 oncology patients selected by block randomization from a large clinical trial were included (457 ± 38 MBq, 64 ± 22 min p.i, body mass index (BMI) of 14–41). Sparse-ring PET configurations with 50 % detector reduction in tangential and axial directions were analyzed and compared to the current full ring configuration. Resulting images were reviewed blindly and quantitatively over detectable lesions and the liver.

Results: One hundred twelve lesions (d = 10 to 95 mm) were analyzed in the patient population. All lesions remained visible and were demonstrated without compromised image quality under all BMIs in the 50 % sparse detector configurations despite the DPC PET system sensitivity reduction to 1/4th. An excellent consistency of SUV_{max} measurements of lesions with an average of 5 % SUV_{max} difference was found between dPET of full and sparse configurations.

Conclusions: The feasibility of either expanding the axial field of view (FOV) by a factor of two or halving the number of detectors was demonstrated for solid-state digital photon counting PET, thus either potentially enabling cost reduction or extended effective axial FOV without increased cost.

Key words: Digital photon counting, Sparse-ring PET, Silicon photomultiplier, Solid state, 2-deoxy-2-[^{18}F]fluoro-D-glucose, Whole-body PET

Introduction

While positron emission tomography (PET)/X-ray computed tomography (CT) has evolved to be an essential non-invasive hybrid molecular imaging technique, its utilization and availability can be limited by its relative high cost compared to other cross-sectional methodologies. Therefore, technological advances may not be able to continuously rationalize higher costs, and innovative approaches maybe essential to create the market acceptance with stable costs while leveraging new technologies for ongoing PET system evolution.

Different types of PET detectors were developed over the last decades, and up to now are predominantly based on the photomultiplier tube (PMT). The recent introduction of solid-state silicon photomultiplier (SiPM) detectors has been another technology leap [1–4]. The new generation of solid-state digital photon counting (DPC) detectors couple directly with cerium-doped lutetium yttrium orthosilicate (LYSO) scintillators which eliminates the need for Anger-logic positioning and decoding [5]. While DPC-based detector PET technology has revealed preferable system performance and improved image quality and diagnostic confidence [6–8], the relative high cost of solid-state detector assemblies and associated advanced electronics make longer axial field-of-view (FOV) designs increasingly expensive.

Correspondence to: Michael Knopp; *e-mail:* knopp.16@osu.edu

Sparse data approaches are increasingly being utilized to accelerate imaging especially in magnetic resonance imaging and CT [9–11]. This pilot study was undertaken to explore whether or not detector configurations of the current DPC PET/CT system (Vereos, Philips) can be reconfigured with reduced number of DPC PET detectors while retaining PET image quality. This is especially relevant if a limited axial FOV could be substantially expanded without additional detector expense. If feasible, an expanded axial FOV without increased costs or reduced costs for the current FOV would be possible.

Rather than physically removing scintillators and DPC detectors from the system, we utilized simulation-based approaches enabled by PET listmode data sets to facilitate virtually modified PET imaging acquisitions using PET sparse-ring detector configurations. This approach enabled us to use clinical oncologic whole-body scans acquired with the full ring DPC PET system within a clinical trial for intra-individual comparative assessment.

Methods

PET/CT System

A next generation, pre-commercial release DPC PET/CT system (dPET) having a 1-to-1 LYSO-to-SiPM coupling was used (Vereos, Philips). The 764-mm PET detector ring spanning 164 mm in the axial FOV is composed of 18 flat detector modules with 4 by 5 array SiPM detector tiles on each module. Every tile consists of 4 × 4 matrix sensor silicon dies with 2 × 2 matrix detector cells (silicon pixel) on each die, and every silicon pixel couples directly to a 3.86 × 3.86 × 19 mm^3 single LYSO crystal with a total of 23,040 (18 × 4 × 5 × 8 × 8) individual and exclusive LYSO-to-SiPM couplings.

Patient

Ten oncologic patients were selected by block randomization from a large clinical trial (NCT03387618) using the selection criteria of (1) must have multiple target lesions and (2) BMI within the following block ranges (five BMI 20–30, two BMI < 20, and three BMI > 30). All patients of the trial had whole-body PET/CT imaging performed on the dPET system before or after their clinical standard of care (SOC) 2-deoxy-2-[^{18}F]fluoro-D-glucose ([^{18}F]FDG) PET/CT. The six females and four males included had a BMI = 27 ± 8 (14–41) with different types of cancer (two rectal, two colon, two lung cancer, two melanoma, one head/neck, and one cervical).

PET/CT Imaging Procedure

[^{18}F]FDG dosing occurred according to the current local SOC protocol (457 ± 38 MBq, 64 ± 22 min p.i.) and imaging was performed using 90s/bed. A water cylinder phantom was used and scanned for uniformity PET imaging (56 MBq [^{18}F]FDG) with 90s/bed for validation. Imaging data was used to evaluate the feasibility of sparse-ring dPET compared to the full ring dPET.

Sparse-Ring PET Simulation

Listmode data was reconstructed (3D time-of-flight (TOF) ordered subset expectation maximization (OSEM), 4 × 4 × 4 mm^3 voxel size) using different detector configurations by excluding events from specific silicon pixels reflecting a sparse-detector ring configuration: (a) the default, fully populated detector; (b) every other silicon pixel removed in tangential direction; and (c) every other silicon pixels removed in axial direction. An example of the schematic diagram of dPET partial detector patterns is shown in Fig. 1.

Image Processing and Data Analysis

The number of coincidence events recorded in the listmode data sets measured as data file size (kilobyte) was used as a

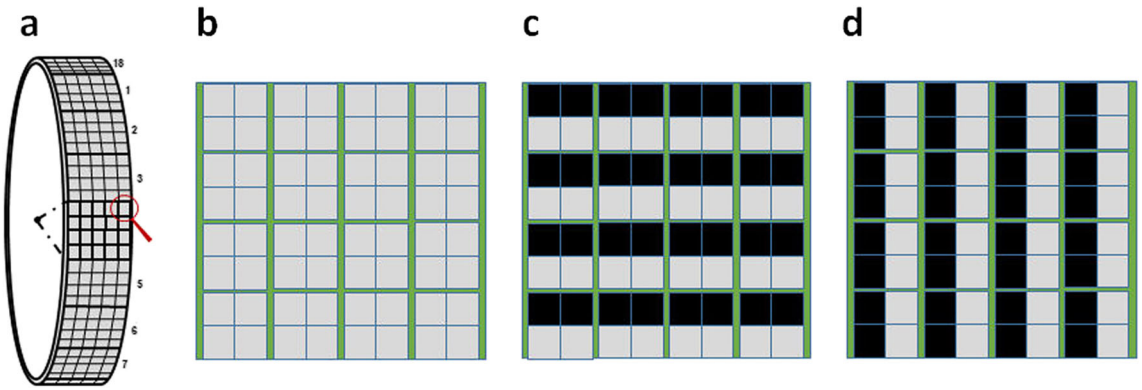

Fig. 1. A schematic diagram of DPC PET detector patterns. **a** The detector rings consist of 18 flat DPC modules with 4 × 5 array SiPM detector tiles on each module, a representative tile (the red magnifier) is zoomed in for **b** the full detector configuration as well as the 50 % sparsity configuration in **c** tangential and **d** axial directions, with silicon pixels disabled and highlighted in black.

proportional surrogate to indicate the change of count statistics under sparse-ring PET configurations. Quantitative standardized uptake value (SUV) assessment of lesions (SUV_{max}) and normal liver tissue (SUV_{mean}) was performed using 3D sphere-based region-of-interests (ROIs) placed by blinded, experienced image reviewers. Sphere ROIs with 30 mm in diameter were placed on normal liver parenchyma. The readers used a 5-point Likert scale (very poor, poor, acceptable, good, excellent) to assess lesion detectability and diagnostic confidence based on the images presented.

After considering corresponding changes of system normalization and SUV calibration, SUV values were calculated and corrected for the sparse-ring dPET configuration and compared to the standard full-ring dPET. SUV differences in percent, system sensitivity, and noise equivalent count rate (NECR) between sparse-ring and full-ring as well as between the two different sparse-ring configurations were evaluated.

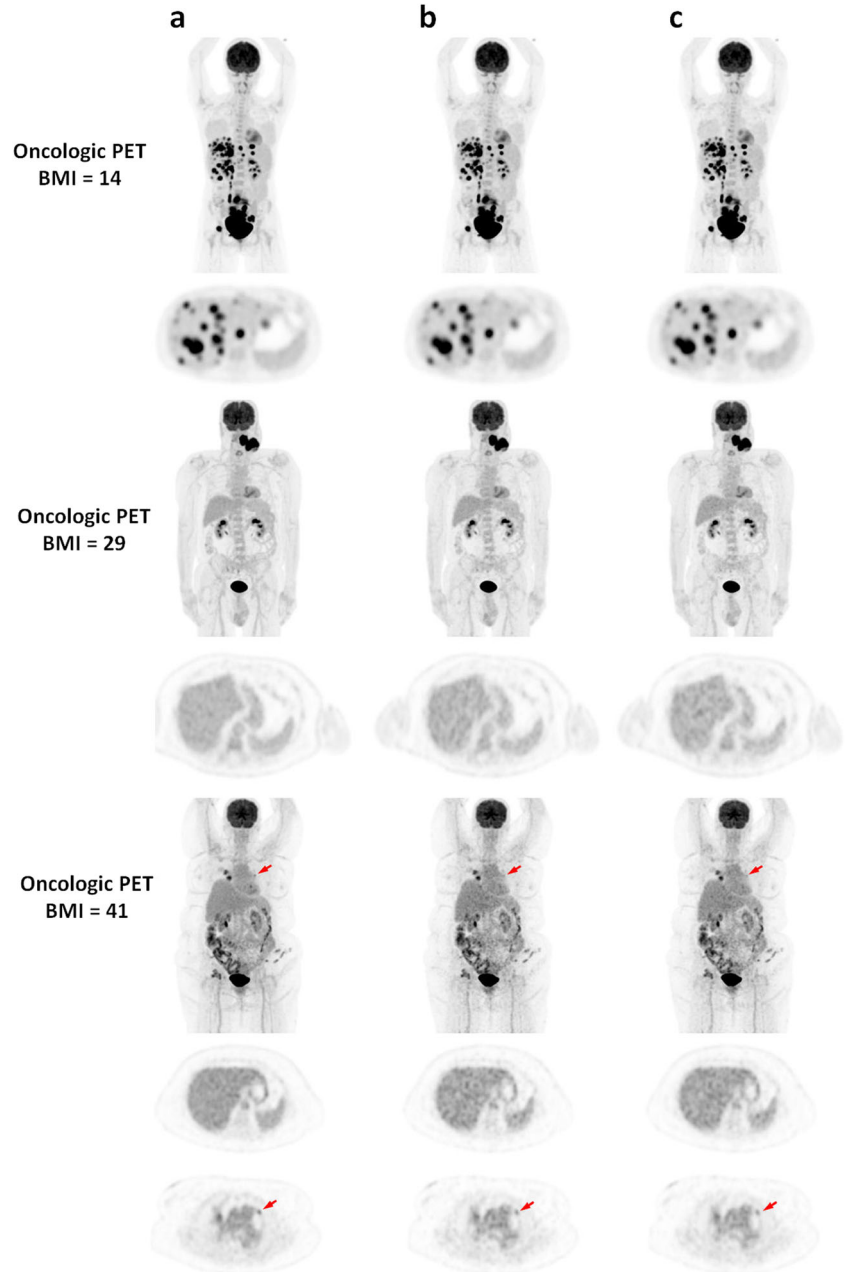

Fig. 2. Intra-individual comparison of whole-body PET acquisitions (480 MBq, 90s/bed) of three patients in vertical direction with different BMI (low to high) using **a** the default full ring detector configuration, **b** 50 % sparse tangential detector, and **c** 50 % sparse axial detector configuration. 3D MIP and axial images are displayed. Excellent image quality is seen for all configurations. The sparse configuration images have a slightly increased noise as expected; however, even a small intrapulmonary metastasis (red arrow, $d = 10$ mm) on the high BMI patient PET remains clearly identifiable on the transverse slices.

Results

One hundred twelve lesions were quantitatively evaluated and visually assessed by blinded review. Compared to the standard fully ring dPET (a), lesions remained clearly identifiable on both sparse-ring dPET configurations (b, c). The 50 % detector reduction approach created by symmetrically disabling every other individual DPC silicon pixel presented excellent and clinically equivalent PET image quality in the read with no apparent/visible artifacts, for both oncologic and phantom PET images.

Figure 2 demonstrates three representative clinical cases (low to high BMI) reconstructed with and without sparse PET detector configurations. The low BMI patient (BMI = 14) had extensive metastatic lesions of varying sizes and intensity in the liver and abdominal region. Reducing the number of detectors to half, did not deteriorate the lesion detectability and diagnostic confidence of the readers. For the average size patient (BMI = 29) with head and neck cancer, tumors in the neck are clearly identified on the sparse-ring dPET configuration without any ambiguity, and with equivalent biodistribution of normal tissues and background. Even in the obese patient (BMI = 41), the sparse-ring configuration dPET presented with clinically acceptable image quality with the majority of lesions identifiable. Two smaller pulmonary lesions appeared to be blurred on the maximum intensity projection (MIP) display; however, they remain confidently identifiable on the cross-sectional images. Consistent with this observation, the images on the sparse detector configuration appear to be slightly blobby compared to the full detector configuration. Similar trends were found when evaluating the liver uniformity which appears to be relatively blobbier in patients with larger BMIs.

The reduced number of detectors caused corresponding count losses along the blocked line of response (LORs) which further impacts the count to Bq/ml conversion. The uniformity phantom PET experiments (Fig. 3) confirmed that the difference of the conversion scale factor is about 4 (full-ring: sparse-ring). By rule of thumb, SUV values of the 50 % sparse-ring dPET configuration can be simply estimated by multiplying the conversion scale factor of 4 to match SUVs of the full ring PET, or by correctly updating the associated SUV calibration table.

In order to assess the potential impact of the sparse detector configuration on the quantitative assessment, we analyzed the lesions and performed a SUV_{max} comparison between the full- and sparse-ring dPET configurations (Fig. 4). The lesion SUV_{max} values ranged from 1.8 to 28.5 [a.u.] for the [^{18}F]FDG avid lesions ranging in unidimensional diameter from 10 to 95 mm. We found overall an excellent consistency despite the sparse configuration with difference on average of -5 ± 7 % SUV_{max} between full and tangential sparse configuration, -4 ± 6 % between full and axial sparse configuration, and 2 ± 7 % between both sparse configurations. The SUV_{mean} measurements of the liver across all patients were nearly unchanged (-1 ± 1 %) with up to 2 % difference between the 50 % sparse-ring and full-ring dPET configurations (Table 1).

Discussion

In recent years, efforts to further advance conventional PMT PET with novel hardware design and advanced reconstruction algorithms were investigated to enhance PET applications [12–16]. While the new generation of DPC SiPM PET has demonstrated superior system performance and image quality compared to PMT PET, its axial FOV (164 mm) is limited by trade-offs due to the high cost of the detector and advanced electronics.

Rather than physically removing and potentially destroying detectors from the tightly packed detector ring assembly, we demonstrated that it is possible and efficient to virtually exclude data from detector locations and thus simulate sparse ring dPET configurations. This simulation-based approach enabled us to challenge the conventional concepts of DPC detector configuration design.

In this study, we evaluated the effect of different sparse-detector ring designs on clinical DPC TOF PET imaging. In order to investigate the boundary conditions and evaluate the minimum required DPC SiPM detector coverage, we examined dPET images reconstructed with reduced DPC-detectors under

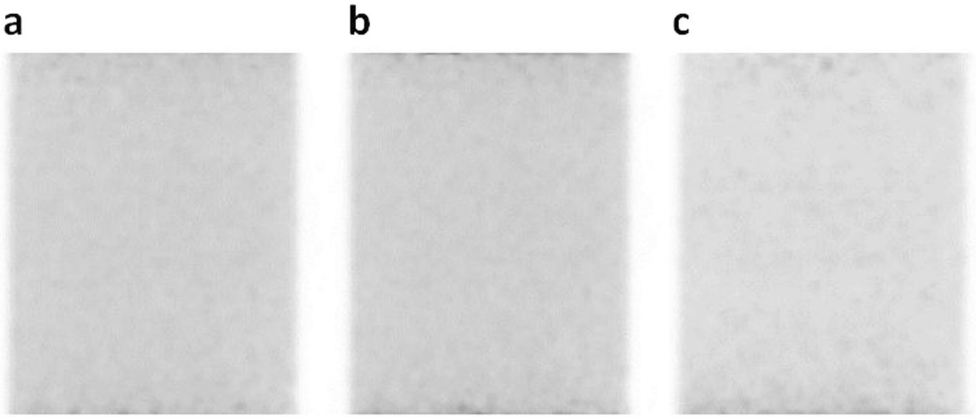

Fig. 3. Uniformity phantom PET (56 MBq [^{18}F]FDG) of **a** full ring detectors and 50 % sparse detector configuration in **b** tangential and **c** axial directions.

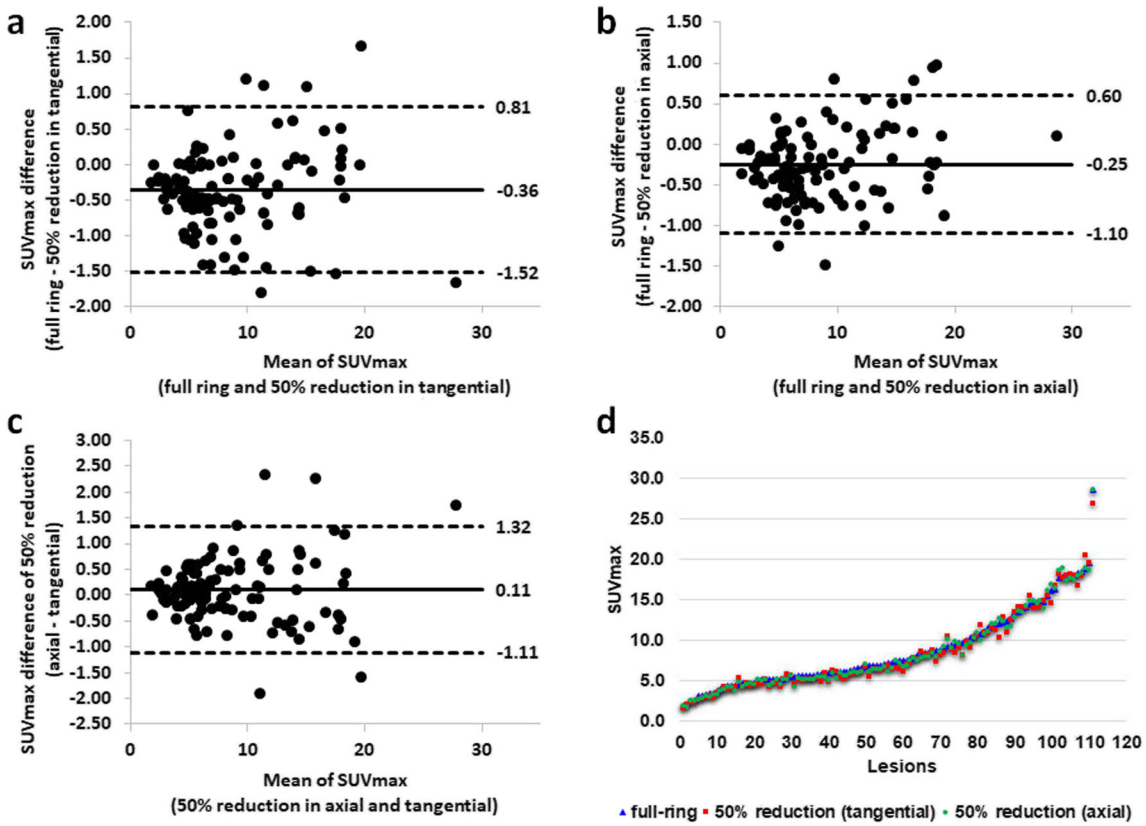

Fig. 4 Comparison of quantitative assessment in SUV_{max} among the full, 50 % sparse tangential and 50 % sparse axial PET configurations based on 112 measureable lesions of 10 oncologic patients whole-body [^{18}F]FDG dPET. It demonstrates the results of SUVmax differences as a function of the mean SUVmax in Bland-Altman plot for dPET between **a** full ring and 50 % reduction in tangential, **b** full ring and 50 % reduction in axial, and **c** 50 % reduction in axial and tangential. **d** The SUV_{max} distribution using the three different approaches. The overall data reveal only minor variations with an average 5 % SUV_{max} difference between the full and sparse ring configurations confirming a quantitative stability remains.

specific sparse-detector ring configurations. Surprisingly, we found on both phantom and clinical oncologic whole-body [^{18}F]FDG PET images that a detector sparsity of 50 % can be implemented without clinically impacting image quality and quantification. The detector cost could be halved using the current FOV coverage. In another words, once this is technically implemented, detectors could be removed from the current design and added in *z*-axis to extend the axial FOV covering more distance without adding cost, thus allowing for shorter exam times or maintained lesion detection when injecting lower activities.

It is worthwhile to look at changes of system characteristics under the sparse-ring configurations, as shown in Table 2. For a sparse-ring configuration implemented by removing half of the detectors symmetrically, the probability of detecting single photons is reduced by one half, thus the probability of detecting paired coincidence photons is reduced to one fourth. As a result, the system sensitivity is reduced to one fourth. This can also be described using the following formula [17–20].

$$\text{Sensitivity} = \varepsilon^2 \frac{A}{4\pi r^2} e^{-\mu T}$$

where ε is the detector efficiency, A is the single detector area seen by a point source to be imaged, r is the radius of detector ring, and μ and T are the linear attenuation coefficient and total thickness of

Table 1. Liver SUV_{mean} measurements using a 30-mm diameter spherical ROIs in the ten oncology patients measured on the full and 50 % sparse detector configurations

	Liver SUVmean (sphere ROI with 30 mm in diameter)									
Patient #	#1	#2	#3	#4	#5	#6	#7	#8	#9	#10
Full ring	1.5	1.6	1.9	2.0	2.2	2.2	2.3	2.8	2.8	3.4
50 % reduction (tangential)	1.5	1.6	1.9	1.9	2.1	2.2	2.3	2.7	2.8	3.4
50 % reduction (axial)	1.5	1.6	1.9	1.9	2.1	2.2	2.3	2.7	2.8	3.3
Difference (avg ± stdev %)	−1 ± 1 %									

Table 2. DPC detector configurations, measured PET list-mode data sizes, and estimated system TOF timing resolution, sensitivity, and NECR of the sparse-ring PET configurations compared to the full-ring PET

DPC PET detector	Relative listmode size (avg ± stdev)	TOF timing (ps)	Relative sensitivity	Relative NECR
Full ring	1	325	1	1
50 % reduction (tangential)	25 ± 0.2 %	Unchanged	1/4	1/4
50 % redauction (axial)	25 ± 0.2 %	Unchanged	1/4	1/4

the object, respectively. By a sparse 50 % detector configuration, the coincidence detection efficiency ε is cut by 50 % while the remaining parameters are unchanged and the system sensitivity proportional to ε^2 is therefore reduced to one fourth. This theoretical consideration was confirmed by the phantom experiments with PET listmode data size changes, as shown in Table 2.

The same consideration applies to the noise equivalent count rate (NECR) which is given by [20].

$$\mathrm{NECR} = \frac{T^2}{T + S + R}$$

where T, R, and S are the true, random, and scatter coincidence count rates, respectively. For the same reason that the probability of paired coincidence photons detection is reduced to one fourth, the true, random, and scatter coincidence events are one fourth of those using a full-ring dPET, and the NECR becomes one fourth for the 50 % sparse-ring dPET.

As the system sensitivity was found to be substantially reduced to one fourth using the 50 % sparse configuration, it is necessary to review why the obtained dPET images still achieved equivalent image quality without interfering with lesion detection when compared to the full-ring dPET. In our view, there are at least two reasons: (1) We believe, for image quality, it is more important to obtain high-quality counts than more lower-quality counts with higher uncertainty. NEMA sensitivity measures only a system's ability to convert photons to raw counts (quantity) and does not take into account the quality of counts. Sensitivity reduction leads to less count quantity instead of quality. For the dPET system, the 1-to-1 coupling design without anger logic decoding provides more accurate annihilation localization of counts, and the substantially improved timing resolution (322 ps) enables a high TOF gain, both improves the quality of counts. (2) The current local SOC [^{18}F]FDG dose administration (481 MBq) is relative high. Our findings based on separate studies demonstrate that a 60–70 % reduction of the dose still leads to good image quality of dPET without compromising lesion detectability. The observations are consistent and relatively equivalent to the reduction of sensitivity resulting from a sparse-ring configuration.

By that analogy, if we double the axial FOV by moving half of the detectors in such sparse configuration and extending them to z-axis along the bore (assume other conditions stay the same and with no impact of solid angles), system sensitivity and NECR would be maintained and unchanged compared to the current full-ring dPET.

The solid-state DPC PET has high-quantum-efficiency photon detection capability which leaps the technology forward compared to conventional PMT PET. The pilot data indicate that the dPET system with its 322 ps timing resolution is very tolerable to compensate for gaps in DPC detector ring geometry, and the timing resolution does not deteriorate as illustrated. To overcome the high cost of expanding in the axial FOV, sparse detector configurations may be utilized for cost-efficiency while enabling expanded z-axis long-bore systems. Depending on the detector pattern used, a reduced number of solid state detectors (e.g., 50 % sparsity) is feasible without clinically relevant reduction in PET image quality or quantification.

One of the study limitations is that we have not evaluated the feasibility of performing sparse-ring dPET using different PET tracers and isotopes.

Conclusion

We introduce the concept that sparse-ring PET configurations using DPC detectors are possible without degrading clinical image quality despite the lower count statistics. The potential clinical impact could either reduced costs of PET systems or improved axial coverage without higher equipment cost, both potentially disruptive advances.

Acknowledgements. Dr. Bin Zhang (Philips) provided technical support.

Financial Disclosure. The study is supported by the ODSA grant TECH 13-060. Philips provided the pre-commercial release system.

Compliance with Ethical Standards. All procedures performed in the study involving human participants were in accordance with the ethical standards of the institutional research committee and the institutional review board approval. Informed consent was obtained from all participants.

Conflict of Interest

The authors declare that they have no conflict of interest.

References

1. Schaart DR, van Dam HT, Seifert S, Vinke R, Dendooven P, Löhner H, Beekman FJ (2009) A novel, SiPM-array-based, monolithic scintillator detector for PET. Phys Med Biol 54:3501–3512
2. Zhang J, Miller M, Binzel K, Tung C, Knopp MV (2016) Evaluation of the stability and system characteristics of digital photon counting PET/CT. J Nucl Med 57(Suppl 2):258
3. Hsu DFC, Ilan E, Peterson WT, Uribe J, Lubberink M, Levin CS (2017) Studies of a next generation silicon-photomultiplier-based time-of-flight PET/CT system. J Nucl Med 58(9):1511–1518
4. Zhang X, Wang X, Ren N, Kuang Z, Deng X, Fu X, Wu S, Sang Z, Hu Z, Liang D, Liu X, Zheng H, Yang Y (2017) Performance of a SiPM based semi-monolithic scintillator PET detector. Phys Med Biol 62:7889–7904

5. Zhang J, Maniawski P, Knopp MV (2017) Effect of next generation SiPM digital photon counting PET technology on effective system spatial resolution. J Nucl Med 58(Suppl 1):1322
6. Vandenberghe S, Mikhaylova E, D'Hoe E et al (2016) Recent developments in time-of-flight PET. EJNMMI Phys 3:3
7. Knopp MV, Binzel K, Nagar V et al (2015) Initial clinical experience using a digital PET detector for whole-body oncologic PET/CT. J Nucl Med 56(Suppl 3):1695
8. Wright CL, Binzel K, Zhang J, Wuthrick EJ, Knopp MV (2017) Clinical feasibility of 90Y digital PET/CT for imaging microsphere biodistribution following radioembolization. Eur J Nucl Med Mol Imaging 44:1194–1197
9. Lustig M, Donoho D, Pauly JM (2007) Sparse MRI: the application of compressed sensing for rapid MR imaging. Magn Reson Med 58:1182–1195
10. Bian J, Siewerdsen JH, Han X et al (2010) Evaluation of sparse-view reconstruction from flat-panel-detector cone-beam CT. Phys Med Biol 21(55):6575–6599
11. Kalke M, Siltanen S (2014) Sinogram interpolation method for sparse-angle tomography. Appl Math 5:423–441
12. Lee E, Werner ME, Karp JS, Surti S (2013) Design optimization of a time-of-flight, breast PET scanner. IEEE Trans Nucl Sci 60:1645–1652
13. Valiollahzadeh S, Clark JW Jr, Mawlawi O (2015) Using compressive sensing to recover images from PET scanners with partial detector rings. Med Phys 42:121–133
14. Tashima H, Yoshida E, Inadama N, Nishikido F, Nakajima Y, Wakizaka H, Shinaji T, Nitta M, Kinouchi S, Suga M, Haneishi H, Inaniwa T, Yamaya T (2016) Development of a small single-ring OpenPET prototype with a novel transformable architecture. Phys Med Biol 61:1795–1809
15. Zhang Z, Ye J, Chen B, Perkins AE, Rose S, Sidky EY, Kao CM, Xia D, Tung CH, Pan X (2016) Investigation of optimization-based reconstruction with an image-total-variation constraint in PET. Phys Med Biol 61:6055–6084
16. Son JW, Kim KY, Yoon HS, et al (2017) Proof-of-concept prototype time-of-flight PET system based on high-quantum-efficiency multi-anode PMTs. Med Phys. https://doi.org/10.1002/mp.12440
17. Saha GB (2010) Performance characteristics of PET scanners. In: Basics of PET imaging: physics, chemistry, and regulations. Springer-Verlag, New York, pp 101–102
18. Budinger TF (1998) PET instrumentation: what are the limits? Semin Nucl Med 28:247–267
19. Cherry SR, Sorenson JA, Phelps ME (2012) Positron emission tomography. In: Physics in Nuclear Medicine, 4th edn. Elsevier Health Sciences, New York, pp 319–321
20. Strother SC, Casey ME, Hoffman EJ (1990) Measuring PET scanner sensitivity: relating countrates to image signal-to-noise ratios using noise equivalent counts. IEEE Trans Nucl Sci 37:783–788